Morphological and microstructural characterizations of the fresh fuel plates for the SEMPER FIDELIS in-pile test

Mira Khair, Nicolas Hibert, Jérôme Allenou, Ahmed Addad, Franck Béclin, Matthieu Touzin, Ann Leenaers, Hervé Palancher, Bertrand Stepnik, Olivier Tougait, et al.

Version of Record: https://www.sciencedirect.com/science/article/pii/S0022311522001520
Manuscript_83fc9b24e7f84f1fe326dd96b7812ea8

Morphological and microstructural characterizations of the fresh fuel plates for the SEMPER FIDELIS in-pile test

Mira Khair[1], François Housaer[1], Nicolas Hibert[1], Jérôme Allenou[2], Ahmed Addad[3], Franck Beclin[3] Matthieu Touzin[3], Ann Leenaers[4], Hervé Palancher[5], Bertrand Stepnik[2] and Olivier Tougait[1*]

[1] Univ. Lille, CNRS, Centrale Lille, ENSCL, Univ. Artois, UMR 8181 - UCCS - Unité de Catalyse et Chimie du Solide, F-59000, Lille, France

[2]Framatome, CERCA, SPL, ZI Les Bérauds, 54 avenue de la déportation, BP 114, F-26104 Romans-sur-Isère, France

[3] Univ. Lille, CNRS, INRAE, Centrale Lille, UMR 8207 - UMET - Unité Matériaux et Transformations, F-59000 Lille, France

[4] SCK CEN, Nuclear Material Science Institute, Boeretang 200, 2400 Mol, Belgium

[5] CEA, DES, IRESNE, DEC, F-13108 Saint-Paul-lez-Durance, France

* corresponding author : Olivier Tougait : olivier.tougait@univ-lille.fr

ORCID: 0000-0001-9114-930X

Abstract:

The UMo/Al dispersion fuel in plate form is considered for the conversion of high-performance research reactors in Europe. In the framework of the UMo fuel qualification program, the SEMPER FIDELIS in-pile irradiation tests aims at consolidating the adequate margin of safety performance by considering several technological solutions associated with the fabrication parameters, such as heat-treatment of the UMo particles, coating with a diffusion barrier material and powder size distribution as some examples. All these parameters, along with the effect of the hot-rolling process were evaluated by means of image processing and detailed microstructural characterizations for fresh samples *i.e.* prior to irradiation tests. Principle macroscopic features of powder batches include the size and shape distributions and coating surface examinations. Microscale investigations explored both the coating and kernel microstructures as well as the interface layer between them. Finally, nanoscale analyses examined the UMo–coating interface. The extensive stresses associated with the hot-rolling process have a significant impact on the deformation of the UMo kernels and the degradation of the coated film. The UMo kernels mostly lost their spherical shape for faceted and elongated shapes whereas three types of film degradations were identified including cracks, chippings and delamination.

Keywords: Low-Enriched-Uranium (LEU), UMo Dispersion Fuel, ZrN, Si, Mo coating, interface layer, SEMPER FIDELIS

1 Introduction

UMo/Al dispersion fuel has been identified as the most promising candidate for low enriched uranium (<20% 235U) fuel conversion for European high-performance research reactors [1,2]. Fuel assembly design typically consists of thin plates comprising U-7 Mo (in wt %) atomised powder dispersed in an Al matrix.

Post-irradiation observations have revealed an important interaction between the UMo particles and the Al-matrix which leads to the growth of an interaction layer (IL). Its specific properties, low adherence on UMo particles, amorphous, low thermal conductivity, high fission gas permeability and large expansion at high burn-up are regarded as the main causes of the reduction of fuel-plate integrity which can lead to pillowing [3–6]. Thus, recent successes of core-shell UMo particles coated with Si, Mo, Zr or ZrN film [7–10] acting as a diffusion barrier to reduce the irradiation enhanced diffusion, have boosted interest in further developing this type of advanced technological powder.

Regarding the UMo microstructure, the initial grain structure undergoes grain subdivision for high fission densities. This results in an increase in defect densities (point defect, dislocation, porosity, inclusion, grain boundary) yielding numerous pathways for promoting percolation of gas bubble networks and finally, fission gas release from the UMo particle [11–14]. Fission gas accumulation in the thin plates can induce blistering. Decrease in the subgrain formation rate can be obtained by optimizing the UMo microstructure, *i.e.*, low densities of initial defects, uniform composition, high purity, large grains, as some examples, which can be achieved by appropriated heat-treatments at the fabrication stage.

The international irradiation campaign, SEMPER FIDELIS (SF) [15, 16] performed recently in BR2 reactor (SCK CEN, Mol, Belgium) aims to investigate the technological benefits of these two solutions, i.e. coating and homogenization on full scale fuel plates up to high fission rates. The post-irradiation examinations, currently in progress will provide a fine description

of the thermo-mechanical and physical behaviors of fuel-plates [16]. In parallel to these analyses, a detailed microstructural characterization of the powders and fuel-plates in as manufactured state, *i.e.* before irradiation, has been undertaken [16–18] to examine the relationship between manufacturing features and irradiation damages. Typically, PIE of UMo/Al dispersed plates focus on localized areas (matrix/coating or coating/UMo kernel interfaces) for selected fissile particles. These precise examinations illustrate perfectly the irradiation damages as function of the burn up yielding a comprehensive description on the origin or consequence of microstructural fuel feature. In the present work, an extented approach is attempted through a statistical analysis of several hundred UMo particles issued from five powders and three fuel-plates selected for the SF neutron irradiation experiments.

The investigations focused on the metrology of the powders at the particle scale as well as chemical and physical properties at the atomic scale, in particular at the interfaces between the fissile UMo alloy, the coating layer and the aluminium matrix. The macroscopic scale is important for fuel-plate manufacturing which is based on powder metallurgy processes [15]. Microscale investigations explored both the coating and kernel microstructures as well as the interface layer between them. Finally, nanoscale analyses were performed on the UMo kernel – ZrN coating interface. The characterizations were mainly carried out using electron microscopy (SEM and TEM) on ZrN, Si or Mo coated UMo particles in free powder form, embedded in an Al-compact and in fuel-plate samples.

2 Experimental methods

2.1 Materials

The U-7Mo core particles were produced by atomisation methods, either using a centrifugal rotation disc [19] (KAERI) or by rotating electrode processes [20] (Framatome/CERCA).

Some powder batches were heat-treated under Ar flow at 1000°C for 1h, before coating by physical vapor deposition (PVD) at SCK-CEN [21]. Coating films were deposited in thin layer of about 1 µm thickness for ZrN and Mo and about 0.6 µm thickness for Si by PVD using optimized experimental conditions as described in [8], except for Si-coated powder sample (4a) for which the coating process was discontinued due to a mechanical failure in the rotational motion. Five different core-shell powders were produced whose main manufacturing features are summarized in Table 1.

Fuel-plate fabrication was performed at Framatome/CERCA following a robust protocol which comprises three main steps, (*i*) the cold pressing of a powder mixture of the fuel particles with different granulometries that are dispersed in an Al-base matrix constituting a green body designated as compact and which is embedded in an Al frame (*ii*) the controlled reduction of the frame by several rolling passes and (*iii*) a blister-test performed at intermediate temperature to ensure the adherence between the various layers and the absence of blistering [15]. A cutout piece of 9 x 28 cm^2 was taken from each fuel-plate for inspection procedures and further analyses.

The particles were examined as free powder, embedded in an Al-compact and in fuel-plate samples as summarised in Table 1. The identification of the fuel powders comprises a number and a letter which refer to the fabrication stage, as-produced (letter a) and after hot-rolling (letter b). For powder samples 1a (SF1) and 5a (SF2), only fine particles (sieving below 40 µm) could be analysed.

Table 1 : Identification and main manufacturing features of the samples

Identification number	Batch	HTT [a]	Coating layer	Powder samples [b]	Plate sample [b]
SF1	CERCA 2017 L1	YES	ZrN	1a	-
SF6	KAERI SFLB8/LB9/LC1-B	YES	98% with ZrN 2% with Mo	2a	-
SF4	KAERI SFLA9/LA10B	NO	ZrN	3a	3b (FIDJ0702)
SF5	KAERI SFLA11/LB1-B	NO	Si	4a	4b (FIFJ0502)
SF2	KAERI SFLB2/LB3-3	YES	ZrN	5a	5b (FIDJ0202)

[a] annealing at 1000°C for one hour.

[b] fabrication stage, letter a stands for as-produced powder, letter b stands for hot-rolled fuel-plate.

2.2 Sample preparation

Free powder samples were prepared by dispersion of powder particles on a double face conductive carbon tape with the help of a system made of a funnel and a watch glass in order to create a cyclone. A homogenous distribution was obtained by dispersal of 3 mg of UMo core-shell powder on a circular tape of 1.2 cm in diameter.

UMo/Al-compacts were prepared from a mixture of aluminium (600 mg) and UMo coated particles (45 mg) which was manually cold pressed with a uniaxial pressure of about 630 MPa maintained for 2 minutes. The resulting compacts which were 10 mm diameter and about 3 mm height, were mounted in a conductive polymer resin for surface preparation and electronic microscopy (SEM).

A 9 x 28 mm^2 portion of full-size plates was cut and introduced in epoxy polymer for cladding removal. The pieces were grinded parallel to the hot-rolling direction until the UMo particles and the Al-matrix appeared. The samples were then dismounted from the epoxy polymer to be introduced into a conductive polymer resin.

The Al-compacts and pieces of fuel-plate were polished in successive steps with SiC abrasive papers of grades up to 1200 mesh, followed by a mirror finish with diamond paste from 6 to 1 µm grain sizes. A final polishing step with a colloidal silica suspension was then performed using a vibratory polisher.

Transmission Electron Microscopy (TEM) lamella was produced from UMo(ZrN) compacts using a 30 kV gallium, dual beam focused-ion-beam (FIB) with a narrow cross-section with decreasing ion currents (2 nA- 100 pA) by ion-milling down to a thickness of approximately 100 nm.

2.3 Characterization methods

2.3.1 SEM-EDS Characterization

Image recording and chemical analyses were carried out using a JEOL JSM-7800F LV Scanning Electron Microscope (SEM) in secondary electron (SE) and back-scattered electron (BSE) modes combined with Energy Dispersive X-ray spectroscopy (EDS) (Oxford Instruments SDD detector, AZTEC 80 mm² spectrometer). The working distance was allowed to vary from 3 to 10 mm and the acceleration voltage was adjusted between 5-20 kV in order to increase the topological or chemical contrast. X-ray distribution maps and EDS quantification were performed using an Oxford Instruments SDD detector, (AZTEC 80 mm² spectrometer) at a fixed distance of 10 mm for an acceleration voltage of 20 kV.

For each powder, the magnification was adjusted to the size of the particles to get constant image resolution with good definition of particle contour, coating and UMo core. Images were acquired at 2560x1920 pixels for 80 seconds. Between 7 and 10 images were collected at very low magnification (about 1280x960 pixels) in order to analyse at least 500 particles of the free dispersed powders. These images were employed for the morphological analyses. Between 10 and 20 images from low to high magnification were recorded on Al-compacts and fuel-plates. These images were used to determine the coating thickness, evaluate the cross-section

morphological parameters and examine the UMo kernel to coating interfaces as well as coating damages. For the coating analysis, SEM images were collected using Gentle Beam mode (GB). This method decelerates incident electrons just before they hit the specimen to reduce the incident-electron penetration and charging of the specimen, so as to observe its top surface. The working distance was fixed at 3 mm and the acceleration voltage was adjusted to 5 kV.

2.3.2 Image analysis

Automatic image analysis was performed with the open source program ImageJ [22] to assess the morphological parameters. After correct conversion of true physical values to pixel size, image binarisation was performed by adjusting the grey level threshold of the area of interest so that U-7Mo kernels, coating layers and the Al matrix can be clearly distinguished. Additional filtering steps were added to eliminate noise and small objects with low pixel surface-area. All particles with a continuous boundary were modelled as ellipses having equivalent area (***A***) and perimeter (***P***), allowing the major ($\boldsymbol{d_{major}}$) and minor ($\boldsymbol{d_{minor}}$) axes to be determined, as well as the circular equivalent diameter (*dEC*) and maximum ($Maxd_F$) and minimum ($Mind_F$) Feret's diameters. As a brief recall, note that, d_{major} and d_{minor} refer to the major and minor axes of the best fitted ellipse defining the particle. Circular equivalent diameter (*dEC*) is the diameter of a circle that has the same area as the projection area of the particle and Ferret's diameters (d_F) refer to the distances between two parallel tangents on the perimeter of the particle. The maximum Feret's diameter, ($Maxd_F$), is the largest distance whereas the minimum Feret's diameter, ($Mind_F$), is the shortest distance. As all powder batches were sieved (particles passing through sieve openings of defined mesh size with square apertures), the minimum Feret's diameter, $Mind_F$ was used as size parameter to characterize the Powder Size Distribution (PSD).

To identify the geometric shapes that best define the particles, four shape parameters were introduced. Given that atomised powders have curved outline profiles (absence of polygonal shape) these new parameters were calculated using parameters mainly defining a circle or ellipse, such as the area, perimeter, major and minor axes and equivalent circle diameter [17].

- ***Circularity***: $Circ. = \frac{dEC}{(P/\pi)}$ (1)
- ***Aspect Ratio***: $AR = \frac{dmajor}{dminor}$ (2)
- ***Convexity***: $Conv. = \frac{dmajor}{dEC}$ (3)
- ***Concavity***: $Conc. = \frac{dEC}{dminor}$ (4)

2.3.3 STEM

Transmission electron microscopy in scanning mode (STEM) was performed using a Thermofisher Titan Themis 300 microscope operated at 300 kV and equipped with a probe aberration corrector allowing (HR)STEM images to be acquired at a resolution of 0.7 Å. STEM-based hyperspectral EDS data were obtained using the super-X detector system equipped with four windowless silicon drift detectors with a high sensitivity for light elements. Images were reconstructed from about a hundred frames which were individually collected with a probe current set at a maximum of 200 pA with a dwell time at 10 µs per pixel.

2.3.4 EPMA

Chemical compositions were measured using Electron Probe Micro-Analyser (EPMA). A Cameca SX 100 equipment with five Wavelength Dispersive Spectrometers (WDS), a probe current of 100 nA and an accelerating voltage of 10 kV were employed.

2.3.5 XRD Characterization

Samples were characterised by powder X-ray diffraction on a Bruker AXS D8 Advance diffractometer with θ-θ Bragg-Brentano geometry in a θ–2θ configuration using filtered

Cu Kα radiation (α1-α2 radiations λ=1.540598 Å and λ=1.54439 Å) equipped with a 1D LynxEye detector. The patterns were measured from 15°−100° in 2θ angle with a scan-step of 0.01° and 0.5 s. The FullProf software suite [23] was used to refine the XRD data using the LeBail method.

3 Results and discussion

The impact of manufacturing processes *i.e.* atomisation process, heat treatment, coating, hot-rolling was evaluated by analysing the coated powder particles at various fabrication steps *i.e*. powder, compact, fuel-plate, using a multi-scale methodology. Main macroscopic features of powder batches comprise the size and shape distributions and coating surface examinations. Microscale investigations explore both the coating and kernel microstructures as well as the interface layer between the UMo particles and the coating. Finally, nanoscale analyses was used to examine the UMo – coating interface. The present section depicts the results at the various scales successively for free powder, compact and fuel-plate samples.

3.1 Morphological and physical characterisations of the coated UMo particles

3.1.1 Size and shape distributions of the coated U-7Mo particles

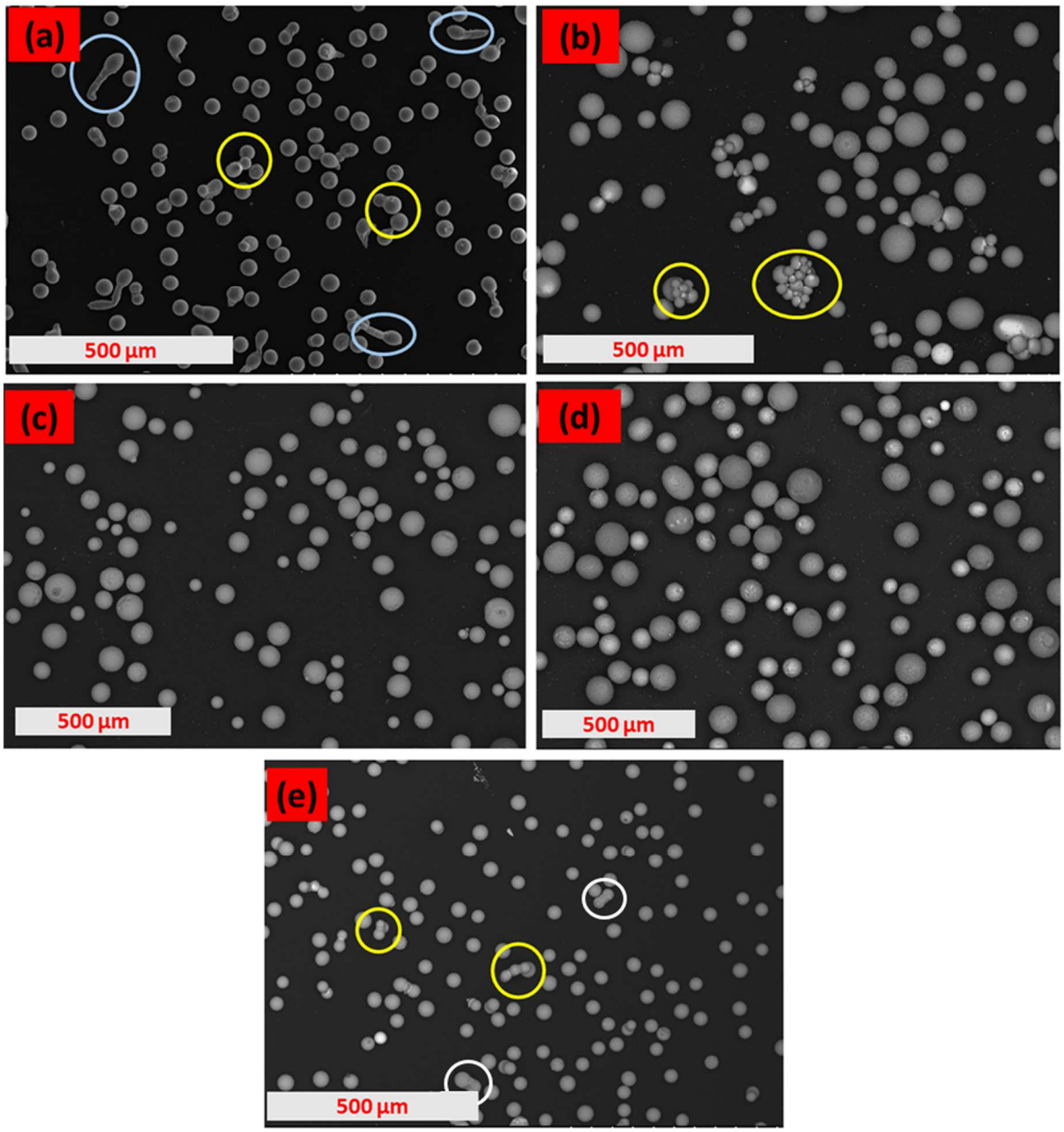

Figure 1: SEM images of U-7Mo powders: (a) Sample 1a, (b) Sample 2a, (c) Sample 3a, (d) Sample 4a and (e) Sample 5a. Blue circles show elongated particles, yellow circles present clusters and white circles signalize peanut shape.

Figure 1 gathers the SEM micrographs in SE mode of the five selected powder samples. It reveals five typical particle shapes: sphere, oval, elongated particle, particle cluster and

unshelled peanut (two connected ovoids). The powder batch 1a, with U-7Mo kernels produced by the rotating electrode process present beside near-spherical particles, some elongated particles corresponding to solidified droplets with a tail (blue circles in Figure 1a). The other powders (2a, 3a, 4a & 5a) which were produced by the centrifugal rotating disk method show rather spherical particles. Powder 2a displays large particle clusters that are highlighted by yellow circles in Figure 1b. A similar tendency of particle agglomeration is visible for powder samples 1a and 5a presented in Figure 1a & Figure 1e, also highlighted by yellow circles. The origin of the cluster formation remains uncertain, but it should be underlined that samples 1a, 2a, and 5a have been heat-treated before PVD coating whereas UMo kernels from samples 3a and 4a, which do not show particle agglomeration, were not. Moreover, ZrN coated films seems to lead to more cohesive powder than Si coated particles when comparing the two none heat-treated samples 3a and 4a which are ZrN and Si coated powders respectively. To illustrate both of these effects on the clustering mechanism, Figure 2 displays cross-section SEM images of ZrN coated UMo kernels. Figure 2a presents two particles bonded by a UMo neck, resulting from the heat-treatment prior to the particle coating (sample 2a) and Figure 2b displays three particles bonded by a ZrN bridge

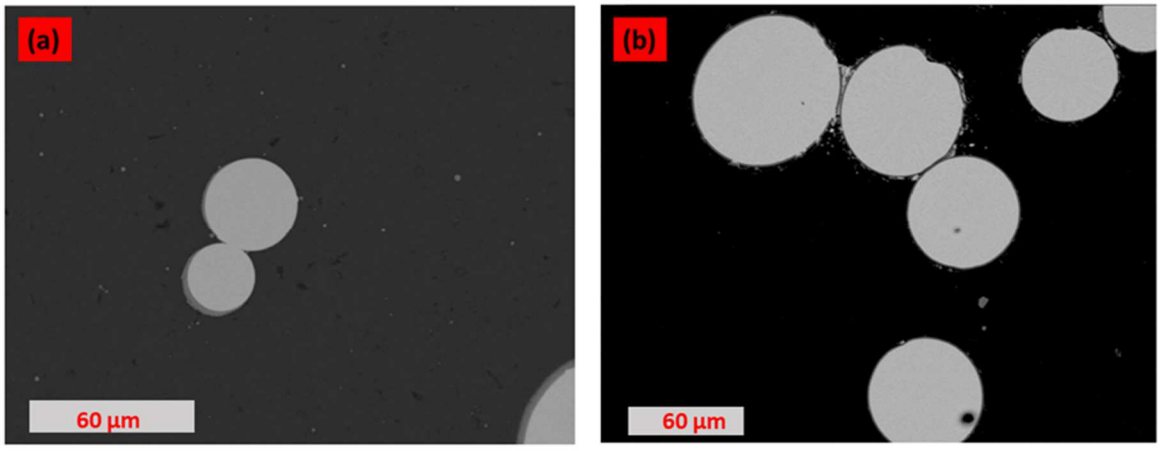

(sample 3a).

Figure 2 : SEM images of U-7Mo connected particles: (a) Sample 2a (two particles bonded by a UMo neck) , (b) Sample 3a (three particles bonded by a ZrN bridge).

Table 2 and Table 3 summarise the main shape and size metrics. Table 2 gives the arithmetic average of the minimum and maximum Feret's diameters, the equivalent circular diameter and the mode (maximum of the frequency distribution) and span ($span = \frac{d90-d10}{d50}$) calculated according to the d_{10}, d_{50} and d_{90} for the minimum Ferret's diameter. Table 3 presents the average shape metrics, aspect ratio, circularity, convexity and concavity. The frequency histograms of the size and shape distributions of each powder batch are presented in the Supplementary Materials.

Table 2: Size metrics (in µm) with the standard deviations for the mean values obtained on free powder.

Powder type	Count	$Mind_F$	d_{EC}	$Maxd_F$	Mode ($Mind_F$)	Span ($Mind_F$)
1a (SF1)	592	36.2 ± 8.3	39.2 ± 11.1	49.0 ± 30.1	32.7	0.37
2a (SF6)	516	61.7 ±14.8	63.1 ± 14.9	68.7 ± 18.1	46.2	0.59
3a (SF4)	622	65.7 ± 17.1	66.3 ± 17.2	69.4 ± 18.1	43.9	0.70
4b (SF5)	566	76.5 ±17.6	77.0 ± 17.9	82.3 ± 19.6	65.0	0.60
5a (SF2)	741	34.7 ± 3.8	35.5 ± 4.0	37.9 ± 5.7	31.0	0.31

The inspection of the particles size distribution bar charts, given in the Supplementary Materials and the average values gathered in Table 2 reveals two feature types of powder size distribution. Powder batches 1a (SF1) and 5a (SF2) have a narrow spread centred around their mode value of 32.67 µm and 30.96 µm, respectively, as expected for fine particles whereas powder batches 2a (SF6), 3a (SF4) and 4a (SF5) have a wider Gaussian distribution expending the range [30 - 120] µm as expected for a powder mixture with fine and medium size particles. The slight extension of the limits compared to the applied mechanical sieving of [40 - 120] µm is attributed to the moderate separation efficiency of the mechanical system for a given sieve opening, of 40 µm and 120 µm.

Table 3: Average shape ratios with their standard deviations obtained on free powder.

Sample code	Count	Aspect Ratio (AR)	Circularity (Cir.)	Convexity (Conv.)	Concavity (Conc.)
1a (SF1)	592	1.38 ± 0.95	0.90 ± 0.10	1.14 ± 0.29	1.14 ± 0.29
2a (SF6)	516	1.12 ± 0.25	0.84 ± 0.06	1.05 ± 0.10	1.05 ± 0.10
3a (SF4)	622	1.04 ± 0.10	0.92 ± 0.02	1.02 ± 0.04	1.02 ± 0.04
4a (SF5)	566	1.05 ± 0.09	0.81 ± 0.04	1.02 ± 0.04	1.02 ± 0.04
5a (SF2)	741	1.07 ± 0.20	0.95 ± 0.03	1.03 ± 0.08	1.03 ± 0.08

For a perfect spherical particle with a smooth surface, all four defined shape parameters are equal to 1. The circularity parameter which is the ratio between the true area reduced to one dimension and the convex perimeter, expresses the degree of roughness of the particle surface. A rough particle with hillocks or attached satellites yields a value less than 1. In line with our previous study on the morphological characterisation of UMo powders coated with ZrN film either deposited by ALD or PVD techniques [17], similar circularity values above 0.90 are obtained for 1a, 3a and 5a samples which correspond to ZrN coated UMo powders. On the other hand, the low circularity value of 2a (SF6) and 4a (SF5) samples (see Table 3) suggests a rough surface for these two powder batches which are ZrN or Mo and Si coated particles, respectively. As illustrated in Figure 3, these two powders display numerous attached spurs and spherules (blue circles). Some hollows are visible for both batches (red

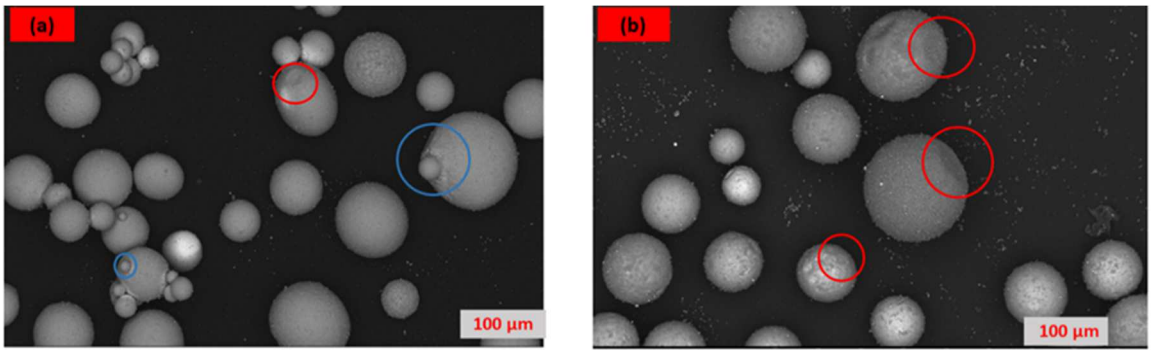

circles in Figure 3) which may be ascribed to solidification shrinkage.

Figure 3: SEM images (SE mode) of U-7Mo powders: (a) Sample 2a, (b) Sample 4a.

The aspect ratio expresses the elongation of the particles and when increasing, the shape evolves from a circle (viewed as a projected sphere), to an ellipse up to an elongated particle. The typical threshold values are 1 for a circle and a near spherical particle can be considered up to AR < 1.1, an oval (spheroid) falls into the range $1.1 \leq AR \leq 1.7$ and an elongated particle has AR > 1.7. Convexity and concavity are also the measures of the degree to which the particle projected shape approaches a circle, but unlike the aspect ratio, they estimated localised shape defaults. The convexity gives the number of particles with any local excess of matter originating from the atomisation or coating processes. The concavity gives the number of particles with at least one flat surface resulting from shrinkage before full solidification or from contact with the walls of the atomisation chamber. Since convexity and concave parameters are related to the diameter of a circle with the same area as the particle projection, similar threshold values between different typical particle shapes can be formulated. For a near perfect sphere, *conv.* or *conc.* should be below 1.05, for an ovoid the value falls into the range 1.05 < *conc.* or *conv.* < 1.1 and for a peanut or large particle cluster, they are above 1.1 going up to 1.5 for adjacent spheres (two spheres in contact at one point). The selected values defining the limits are illustrated in the Supplementary Materials, by giving typical shape ratios for representative objects.

Combining the four shape parameters within each powder batch, allows the different particle geometries that were deduced from the visual inspection, the be identified and counted:

- Spherical and near spherical particles are defined with AR < 1.1 and *conc.* or *conv.* < 1.05

- Oval particles are defined with $1.1 \leq AR < 1.3$ and $1.05 \leq conc.$ or $conv. < 1.1$
- Cluster particles are defined with $1.3 \leq AR < 1.7$ and $1.1 \leq conc.$ or $conv. < 1.5$
- Peanut particles are defined with $AR \geq 1.7$ and $1.1 < conc.$ or $conv. \leq 1.5$
- Elongated particles are defined with $AR > 1.7$ and $conc.$ or $conv. > 1.5$

Table 4 gathers the shape distribution between the 4 selected particle geometries for the five powder batches. Samples 3a, 4a and 5a can be regarded as composed of spherical and near-spherical particles whereas samples 1a and 2a have a significant amount of elongated and cluster particles. For sample 1a, it may suggest that atomisation using the rotating electrode process may promote the formation of elongated particles unlike the centrifugal process, whereas for sample 2a, which contains 2 % of Mo coated particles only, particle agglomeration is abnormally developed. A second point should be underlined and that is that peanut particles and clustering are observed for heat-treated powders, only. It suggests that the annealing initiates the formation of sintering necks that are afterwards consolidated by the deposited matter during the PVD coating.

Table 4: Particle shape distribution (percentage) for UMo powders in Al compact.

Powder type	Count	Spherical and near spherical (%)	Ovoid particles (%)	Peanut particles (%)	Cluster particles (%)	Elongated particles (%)
1a (SF1)	591	70	6	7	7	9
2a (SF6)	516	80	7	4	8	1
3a (SF4)	622	93	6	0	0	0
4a (SF5)	566	91	6	0	0	0
5a (SF2)	741	93	2	4	1	0

3.1.2 ZrN coating: thickness and morphology

The thickness of the coating (th(shell)) was also estimated by image processing. The proper adjustment of the grey level allows two areas to be determined, one larger, comprising the

UMo core and the coating film, namely, A(UMo(shell)) and a second smaller one considering the UMo core, A(UMo), which were both converted to their equivalent circle diameters (*dEC*). The coating thickness (th(shell)) is obtained from the difference between the equivalent circular diameter of the two different areas (equation (5)). An additional filter was applied to remove the peanut, cluster and elongated particles in order to retain only the spherical, near-spherical and ovoid particles. Also, to prevent overestimation of the thickness resulting from the mix-up between chord length and real diameter values [24], the calculations were limited to UMo coated particles which have an observed *dEC* between dEC_{10} and dEC_{90} deduced from the particle size distribution realized on free dispersed powder (see subsection 3.1.1).

$$\text{th(shell)} = \frac{(dEC(UMo(shell)) - dEC(UMo))}{2} \quad (5)$$

Scatter plots of the apparent coating thickness (th(shell) as a function of the dEC are presented in Figure 4 for the five powder batches. The red lines stand for the particles at their real diameter depicting the increase of the coating thickness values with the increase of the U-Mo substrate diameter as previously demonstrated [17,25]. Table 5 presents the average thickness as a function of the particle size range with a bin of 15 µm.

Table 5: Average measured thickness of coatings on the U-7Mo particles, based on the trend associated with the lowest values for a given range of kernel sizes (in µm) [a].

Powder type	[30-45[(µm)	[45-60[(µm)	[60-75[(µm)	[75-90[(µm)	[90-105[(µm)	[105-120] (µm)
1a (SF1)	0.60	0.97	-	-	-	-
2a (SF6)	0.20	0.25	0.31	0.54	-	-
3a (SF4)	0.31	0.33	0.51	-	-	-
4a (SF5)	0.31	0.34	0.42	0.44	0.49	0.53
5a (SF2)	0.53		-	-	-	-

[a] the range a ≤ *th*(shell) < b is written as [a – b[.

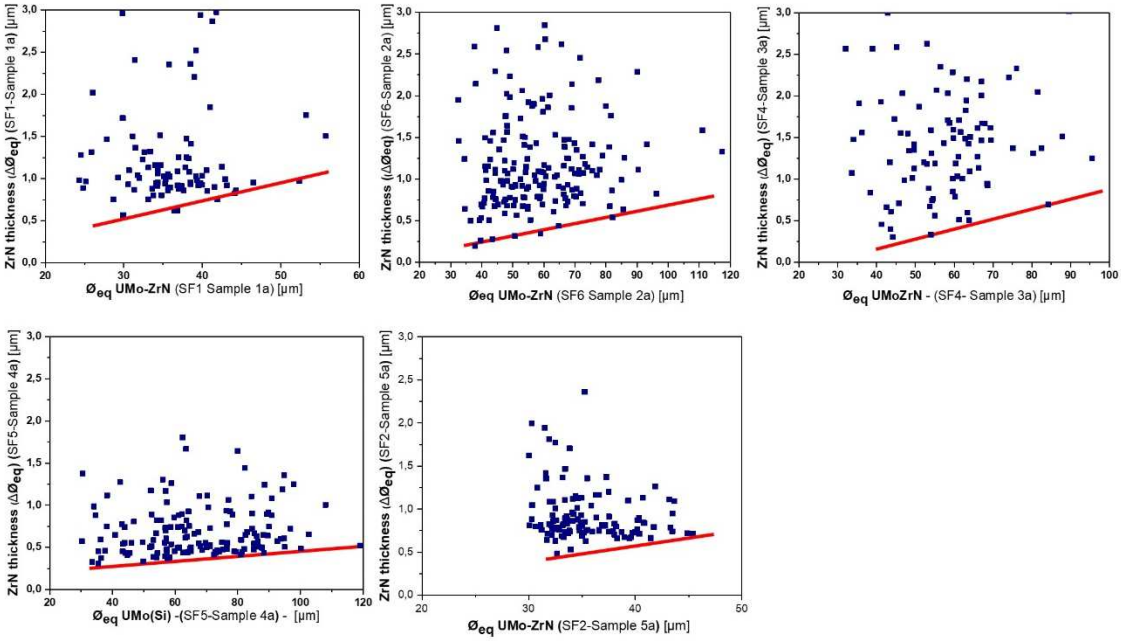

Figure 4: Coating thickness distribution of powder samples (a) sample 1a, (b) sample 2a, (c) sample 3a, (d) sample 4a & (e) sample 5a. The red lines stand for particles at their real diameter.

The radial coating thickness of the UMo powder produced using centrifugal atomisation (batches 2a, 3a, 4a, and 5a) extends over the range [0.3 – 0.6] whereas the ZrN thickness of the UMo powder produced by rotating electrode extends over a range with slightly higher values [0.5-1.0].

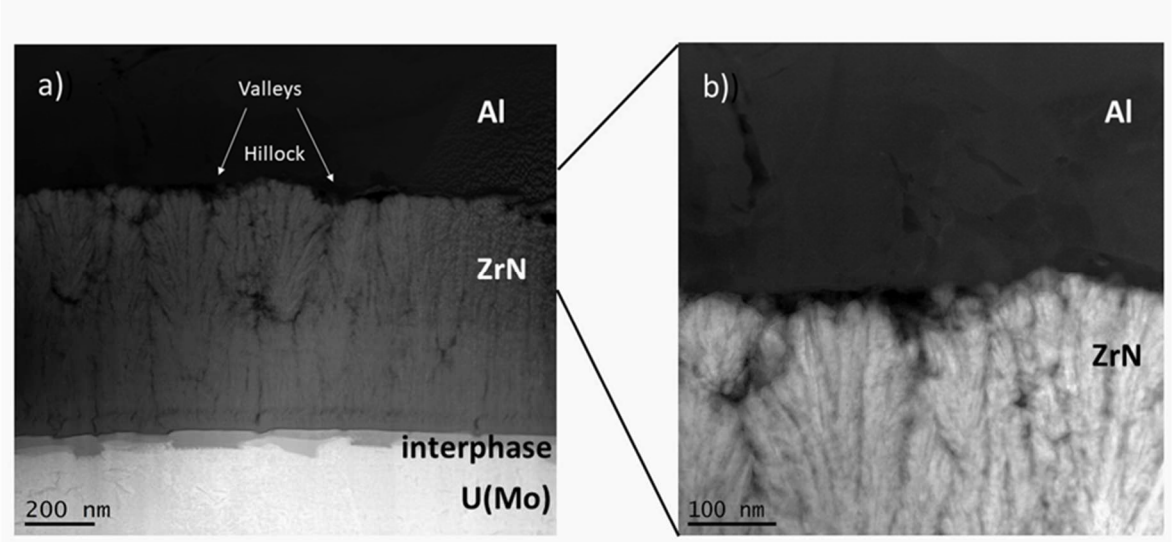

Figure 5: HAADF-STEM micrographs in SF4 (sample 3a) of the approximate position of the UMo-cladding interface.

HAADF-STEM micrographs of the outer part of a UMo(ZrN) core-shell particle are shown in Figure 5. The fibbed lamella was produced from the SF4 powder. In line with the previous observations [25–27], typical ZrN-coating microstructural features are revealed by the TEM imaging. The ZrN film displays a two-sublayer stratified structure, composed of a dense slab underneath a porous slab. The high magnification image exhibits a fine dendritic grain-structure with a sponge-like (fractal) morphology. The dendritic growth yields a highly fibrous network which mainly develops parallel to the growing direction (normal to the surface). These primary arms with lengths from about 5 to 10 nm, arrange themselves with a strong misalignment leading to a porous zone.

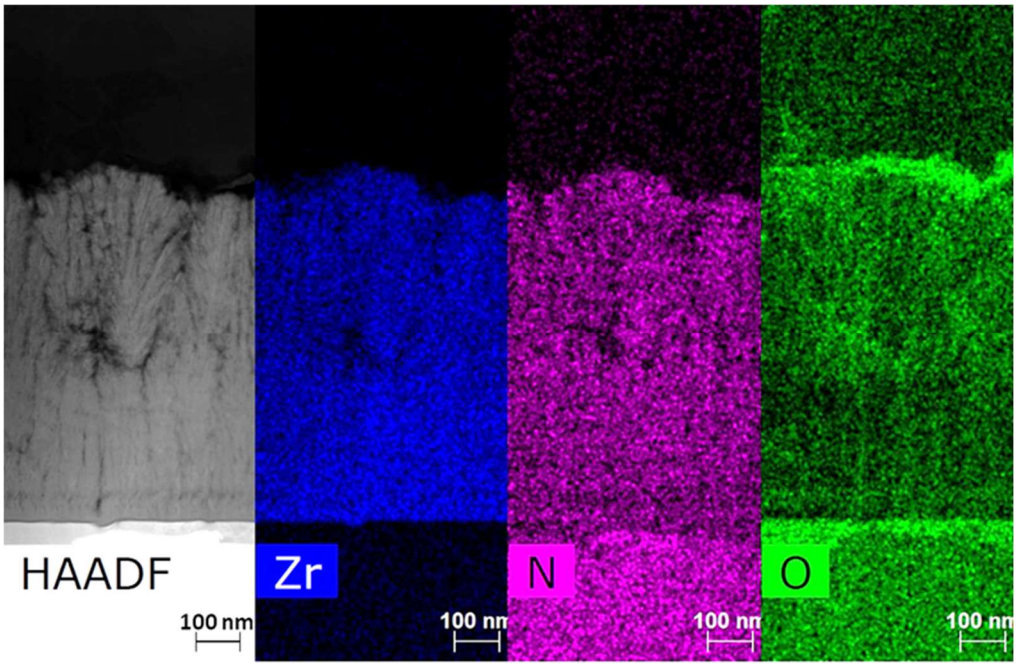

Figure 6: HAADF-STEM micrograph and STEM-EDS X-maps showing the element distribution of Zr, N, O at the UMo-cladding interface collected at 300 kV on SF4 (sample 3b).

Figure 6 shows the associated EDS maps of Zr, N and O. Both the Zr and N are equivalently distributed within the coating film, whereas oxygen is preferentially located in the porous regions, either in cavities or between the ZrN agglomerates. Two areas are revealed depending on the oxygen content, an upper sublayer, close to the Al-matrix, showing high oxygen concentration and a lower sublayer, close to the UMo Kernel showing low oxygen concentration. The separation between these two sublayers can be estimated at about 200 nm from the UMo surface. This value is in line with the previous observations made on various UMo(ZrN) batches [27,28] suggesting a constant feature associated with the coating method and film deposition conditions.

The grain-structure of the coating is mainly dependent on the deposition conditions and especially from the flux rate for the PVD technique, but also from the deposited material itself. Figure 7 presents high magnification SEM images in GB (Gentle Beam) mode of the

coating layer of all of the samples. Figure 7.a, b, d & f correspond to the ZrN coating, revealing porous coated films as depicted previously. Nano-radial and lateral cracks as well as dimples can be observed, including at the film-substrate interface. These cross-section images reveal local stratification within the PVD deposited layer. The PVD coating microstructure consists of cellular crystals stacked along the growing direction and forming particle bulging on the surface.

Mo coating is shown in Figure 7c revealing a fibrous columnar structure of the film, which displays small porosities along vertical boundaries in between individual columns. The column tips exhibit growth facets that are clearly visible on the fractured Mo film. The Mo-UMo interface depicts a sharp boundary suggesting good adhesion strength. Si coating (Figure 7e) exhibits a film structure composed of a dense columnar layer in the vicinity of the substrate overlaid by micrometric spherules. Large porosities are visible between the aggregates and the columnar layer suggesting weak adherence of these spherules with the substrate. Such unusual Si-film behaviour is attributed to the interruption of the coating process (see 2.1 subsection). Like for the Mo-UMo interface, that for Si-UMo displays a continuous and firm bonding. The good adhesion strength and the columnar morphology of both Si and Mo films suggest an epitaxial growing.

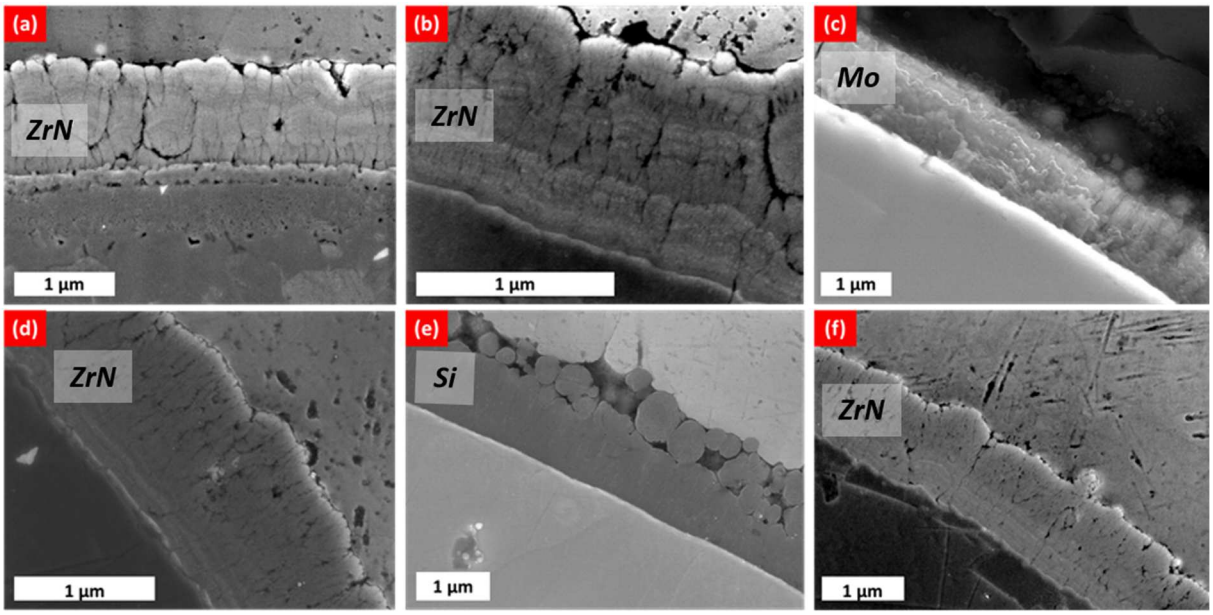

Figure 7: SEM images (GB mode) of several coating on compact samples: (a) Sample 1a, ZrN coating (b) Sample 2a, ZrN coating, (c) Sample 2a, Mo coating, (d) Sample 3a, ZrN coating (e) Sample 4a, Si coating and (f) Sample 5a, ZrN coating.

3.1.3 UMo kernel: as-solidified and annealed microstructures

It is expected that atomised UMo powders will have a complex and versatile microstructure depending on the observed particles and their thermal history. It is common to describe the microstructure of as-solidified atomised UMo powders as a cellular microstructure composed of equiaxed dendrites with some columnar grains at the periphery of the particles [17,29,30]. The metallurgical grains exhibit highly variable sizes, from submicron (0.3 µm) to about ten microns (~ 10 µm) and Mo segregation resulting from fast solidification. Diffraction experiments either using electron (EBSD), neutron or synchrotron beams indicate that γUMo is the unique crystallised phase [14,29,31]. The heat-treatment performed will yield a more uniform microstructure characterised by large polygonal grains, most of them being equiaxed grains. A uniform Mo distribution is measured within almost the whole grain, with the exception of a thin layer in the vicinity of the UMo core surface [26,30,32,33]. Along with the grain growth, strain and stress relaxations are expected from the annealing with beneficial effects on defects and annihilation of dislocations.

The effect of the heat treatment on the microstructure of UMo cores was conducted by EPMA and metallographic observations using both electronic and light microscopies. These two techniques allow the chemical segregation and the grain morphology to be assessed and typical images were obtained for the 5 powder batches. In line with the previous results, the as-solidified microstructure displays separation defining cellular to columnar grains a few micrometres in size. The annealed UMo microstructure is homogeneous with both a uniform distribution of the chemical constituents and a grain structure which shows equiaxed grains of several tens of micrometres. Selected optical and electronic images as well as the X-maps provided by EPMA or EDS are given for all powder in the Supplementary Materials.

3.1.4 UMo kernel - coating layer interface

Micro-analyses, mainly those carried out on annealed UMo batches, show a fine and irregular zone at the interface between the UMo kernel and the coating film that would be enriched in uranium. The presence of this layer has already been reported in the literature [16,18,26,28,30,32,33]. It is described as a superficial layer of oxidation resulting from the chemical interaction of the UMo powder with residual oxygen from the atmosphere during the atomisation process [28,31,33] or from the heat treatment [16,18]. This oxide layer regarded as UO_2 [18,26,33] is also believed to play an important role in the adhesion of the deposited film on the UMo core [26,33]. The HAADF image showing the interface region between the annealed UMo kernel and the ZrN coating along with the EDS compositional analysis of the various layers are presented in Figure 8**.** The measurements were carried out as point analysis in the UMo kernel (Spectrum 1), the interface slab (Spectrum 2) and in the ZrN coating (Spectrum 3) and were repeated 3 times for each location, giving reproducible results.

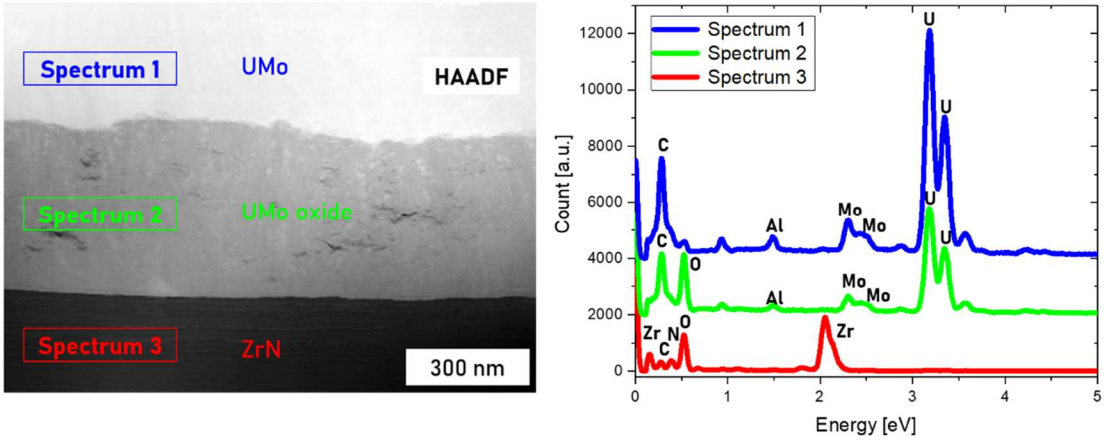

Figure 8: STEM-HAADF image and EDS spectra from three different regions showing the elemental distribution of U, Mo, Al, Zr, N, O in sample 3a (SF4). The Cu peaks in the EDS spectra 1 & 2 come from the Cu grid sample holder and the Al peaks in spectrum 1 & 2 are present due to the redeposition of Al during the preparation of the fibbed lamella

The comparison of the three EDS spectra allows the interface region to be better described in terms of chemical composition. Spectrum 1 recorded in UMo, displays U, Mo and C along with minute traces of O. This layer shows the highest C concentration and the lowest O content. Spectrum 2, recorded in the intermediate layer shows U, Mo, C and O, the two light elements being almost in equal concentration. The enrichment in O is the signature of the oxidation of the UMo skin as already claimed. However, the presence of C and Mo suggested that this slab contains several phases, not only UO_2. According to the chemical composition and comparable analyses carried out on UMo foil [34], the presence of a carbide or an oxy-carbide phase can be forecasted, as well as an uranium nitride phase as recently suggested [16]. Regarding the proximity of the emission line of these three light elements and recurrence of oxygen contamination of uranium carbo-nitride phase [35], this phase is described as U(C,N,O). Spectrum 3 shows Zr, O, N as determined on the EDS maps presented in subsection 3.1.2 and as expected for the ZrN deposited film. Few traces of C are detected. The C origin remains undetermined but may be ascribed to minute pollution during the various

preparation steps, production of the particles or preparation of the sample, or to CO_2 molecules physically adsorbed on the lamella surface.

Powder X-ray analyses using a conventional laboratory diffractometer were collected for the 5 powder samples, amongst which 3 are with annealed UMo kernels (samples 1a, 2a and 5a) and 2 with as-atomised UMo kernels (samples 3a and 4a). The results of the full pattern Lebail refinement fit are gathered in Table 6.

Table 6: Crystallographic phase identification based on cell parameters (Å) and unit-cell volume (Å^3) obtained from the LeBail refinement for samples 1a, 2a, 3a, 4a and 5a

Crystalline phase	Space group	1a (SF1) HTT	2a (SF6) HTT	3a (SF4) no-HTT	4a (SF5) no-HTT	5a (SF2) HTT
UMo	$Im\bar{3}m$	*a*=3.437(1) V= 40.58(1)	a=3.435(1) V=40.54(1)	a =3.434(1) V=40.48(1)	a=3.435(1) V=40.54(1)	a =3.435(1) V=40.52(1)
ZrN	$Fm\bar{3}m$	a =4.595(1) V=97.04(1)	a =4.590(1) V=96.67(1)	a =4.587(1) V=96.51(1)	-	a =4.586(1) V=96.43(1)
Si	$Fm\bar{3}m$	-	-	-	Cannot be refined [a]	-
UO_2	$Fm\bar{3}m$	a=5.482(1) V=164.74(1)	a =5.479(1) V=164.43(1)	a =5.503(1) V=166.67(1)	Cannot be refined [a]	a = 5.472(1) V=163.83(1)
U(C,N,O) #2	$Fm\bar{3}m$	a = 4.909(1) V=118.28(1)	a =4.911(1) V=118.47(1)	Not-observed	Not observed	a =4.906(1) V=118.06(1)
U(C,N,O))#2	$Fm\bar{3}m$	a = 4.945(1) V = 120.91 (1) Å^3	a = 4.946(1) V = 121.02(1)	Not-observed	Not observed	a = 4.946(1) V=121.01(1)
Al	$Fm\bar{3}m$	a=4.051(1) V=66.47(1)	a=4.050(1) V =66.44(1)	a=4.049(1) V=66.40(1)	Cannot be refined [a]	a = 4.049(1) V =66.40(1)
χ^2	-	1.62	1.56	1.96	2.11	1.63

[a] small contribution emerging from the background, but of too low intensity to be refined.

In agreement also with previous crystallographic examination of Si and ZrN coated U–Mo atomised particles [32] typical diffraction peaks featuring γUMo (cI2, W-type), UO_2 (cF12, CaF_2-type), U(C,N,O) (cF8,NaCl-type) and Al (cF4, Cu-type) crystalline phases were indexed and successfully refined for most samples. The refined UMo cubic lattice-parameter, *a* ~ 3.435 (1) Å, is in agreement with typical reported values for U-7Mo [29]. The presence of a fluorite phase is detected for all the diffractograms, but with weak intensities for the as-

atomised UMo kernels, suggesting a very low content of this phase. In comparison, for the samples with the annealed UMo kernels, the fluorite phase was refined, leading a cubic lattice parameter (a ~ 5.48 Å) in agreement with the usual UO_2 values [36]. Similarly, the diffractograms with annealed UMo kernels (samples 1a, 2a, 5a) show typical diffraction lines of a NaCl-type (cF8) adopted by UC and UN crystalline phases [37]. Careful examination of the peak-profile and peak-position, reveal a spacing of the diffraction lines that cannot match with the kα1/kα2 separation, but with the contribution of two isotype crystalline-phases having a distinct cell-parameter. The whole profile refinement using pattern-matching yielded two parameters having for approximate values, *a*U(C,N,O)#1 ~ 4.91 Å and *a*U(C,N,O)#2 ~ 4.95 Å falling in between the lattice parameters of pure uranium carbide and uranium nitride range (UN, a ~ 4.88 Å and UC, a = 4.96 Å) [38] suggesting possible C- and N- rich phases with possible insertion of oxygen atoms into the structures.

It should be underlined, that despite an apparent higher concentration in C in the UMo kernel (spectrum#1, Figure 8) than in the interface slab (spectrum#2, Figure 8), the NaCl-type, UC crystalline phase, is not detected for the un-annealed (as-solidified) samples. It may suggest that the heat-treatment activates C diffusion from the central part towards the outer part of the UMo kernels resulting in the formation of a uranium carbide or oxycarbide phase. Moreover, a Mo containing phase has to be present in the interface layer (spectrum#2) but our crystallographic study carried out with the help of conventional X-ray diffractometry (laboratory powder X-ray diffractometer using kα1/kα2 radiation) failed to provide further insight about its speciation. Further analyses have to be carried out to clarify these uncertainties.

ZrN coated powders (samples 1a, 2a, 3a and 5a) show diffraction lines featuring this crystalline phase but with a broadened profile and a Lorentzian shape as expected for nanosized crystallites [17,26]. On the other hand, the Si coated UMo powder does not show

any appreciable diffraction lines that can be attributed to this element, suggesting that the Si coating is amorphous as already reported in previous analyses [32].

3.2 Fuel plates

3.2.1 Fuel plate examination

The three fuel-plate samples studied, were produced using the conventional process employed at Framatome/CERCA [15] with powder batches 3a, 4a, and for 5a. They are now designated as 3b, 4b and 5b, for the fuel-plate samples. The complete designation of the powder batches is given in Table 1. The fuel-plate samples were examined by using light and electronic microscopies and the chemical analyses were carried out by EDS and EPMA. These classical analyses at the micrometric scale indicate that the hot-rolling (HR) process (*i*) does not induce chemical interaction between the components and (*ii*) does not produce significant evolution of the UMo kernel microstructure for both as-solidified and annealed samples. As presented in the Supplementary Materials, the microstructural description in terms of chemical analyses and UMo grain structure is comparable to that of the compacts. However, grain subdivision or recrystallisation effects associated with the HR process cannot be excluded. Further studies have to be launched to quantify the dislocation densities as an example.

Selected SEM images of the three fuel-plates for several magnifications are presented in the Supplementary Materials as well as in Figure 10. The first point to notice is the significant deformation of the fuel particles which have mainly lost their spherical shape. Three distinct UMo kernel shapes are proposed as rounded, flattened and elongated which correspond to particles with the absence of a flat edge, with at least one flat edge and with two parallel edges, respectively. Outlines of these particles are sketched in Figure 9.

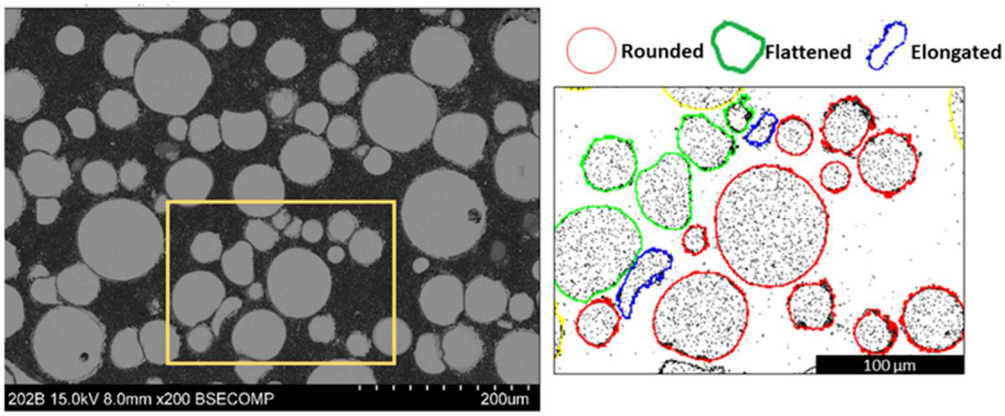

Figure 9: SEM image of 5b sample with the associated binary image outlining the three identified shape particles, rounded (red), flattened (green) and elongated (blue).

The second remarkable point is the detachment of coating fragments into the matrix, which was not visible in the compact samples, excluding the grinding and polishing steps as the main cause of the coating degradation. Three different cases can be considered corresponding to pullouts from the coating film, cracks down to the UMo kernel (blue rectangle) and coating delamination (red rectangle), as depicted in Figure 10.

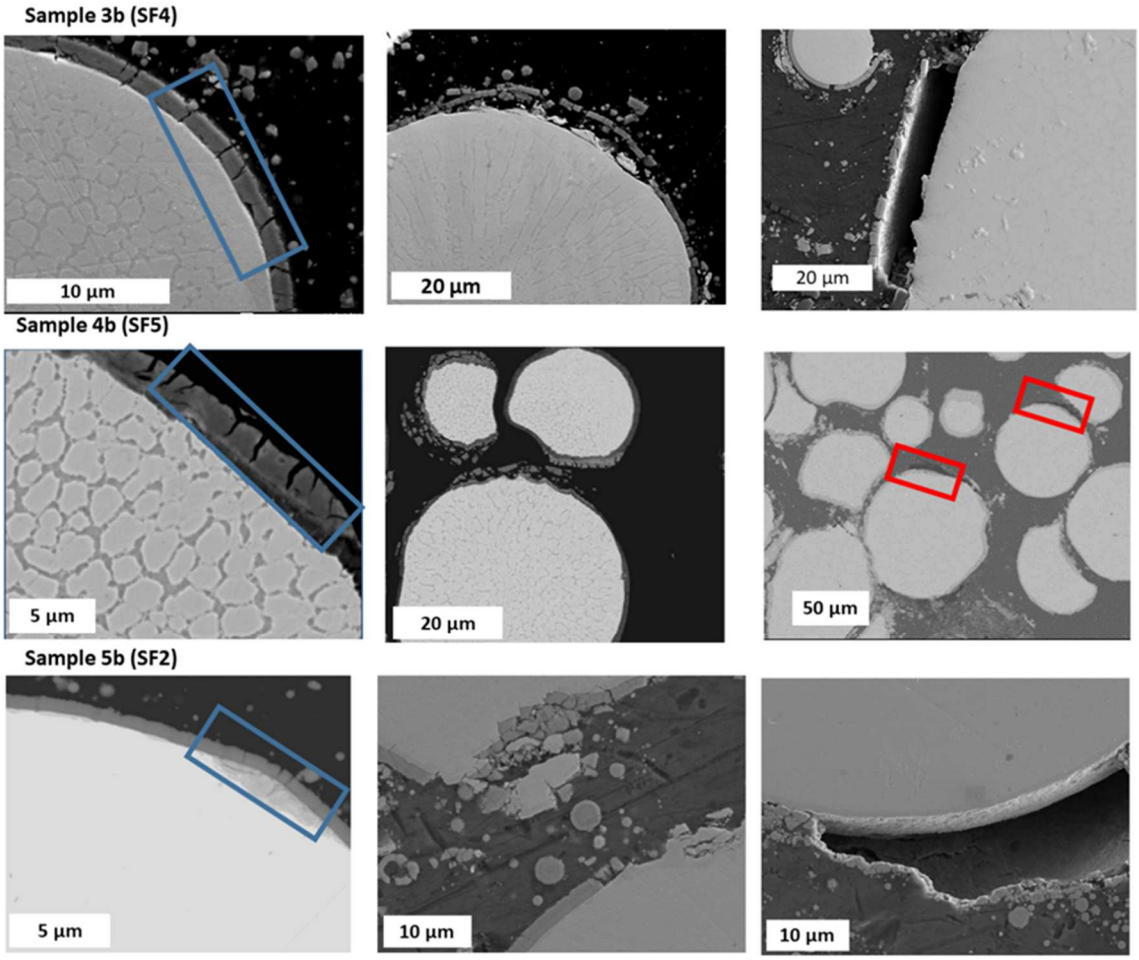

Figure 10: SEM micrographs of U-7Mo plates: showing coating's (ZrN and Si) degradation and delamination. Samples 3b and 5b are ZrN-coating, (top and bottom images) and sample 4b is Si-coating (middle images).

3.2.2 Morphological characterisation: evolution of U-7Mo kernels with hot-rolling

The evolution of particle morphology with the HR process was assessed by using an automatic procedure using ImageJ software. Comparison of the shape factor histograms for the particles within the compacts and within the fuel-plate samples are presented in the Supplementary Materials. They show that the four shape parameters (*AR, conv., conc.,* and *cir.*) are greatly affected, with a spread of the distributions of the values. The three identified shapes: rounded, flattened and elongated has been converted to AR, convexity (*conv.*) and concavity (*conc.)* factors, yielding the following classification:

- Rounded particles: AR < 1.10; *conv.* and *conc.* <1.05
- Flattened particles or random shape: particles with at least one flat edge, 1.10 ≤ AR < 1.7; 1.05 ≤ *conv*. and *conc.* < 1.30
- Elongated particles: loss of curved shape; AR ≥ 1.7; *conc*. and *conv.* ≥ 1.30.

Table 7: Particle shape distribution (percentage) for UMo powders in fuel-plate samples.

Fuel-Plate	Count	Rounded particles (%)	Flattened particles (%)	Elongated particles (%)
3b (SF4)	473	48± 2	47± 2	5± 2
4b (SF5)	419	40± 2	55± 2	5± 2
5b (SF2)	463	48 2	47± 2	5± 2

The new particle distribution reveals approximately an equal partition between rounded and facetted shapes for the ZrN coated UMo kernels with a minority of elongated particles. The Si coated UMo particles display a population mostly composed of facetted particles. This feature is possibly related to the abundance of hollows resulting from solidification shrinkage observed for the powder free sample (powder 4a in subsection 4.1) and which may constitute easy zones for deformation.

The circularity factor was also determined; its distribution for the 3 fuel-plate samples is presented in Figure 11 as histograms. They show a significant widening of the distribution with values centred on 0.82 (3), 0.78 (3) and 0.50 (3) for plates 3b, 4b and 5b, respectively. This factor which depicts the contour of the UMo particles confirms the fractured circumference of the UMo particles. The HR process especially affects the 5b sample which was prepared using annealed UMo kernels.

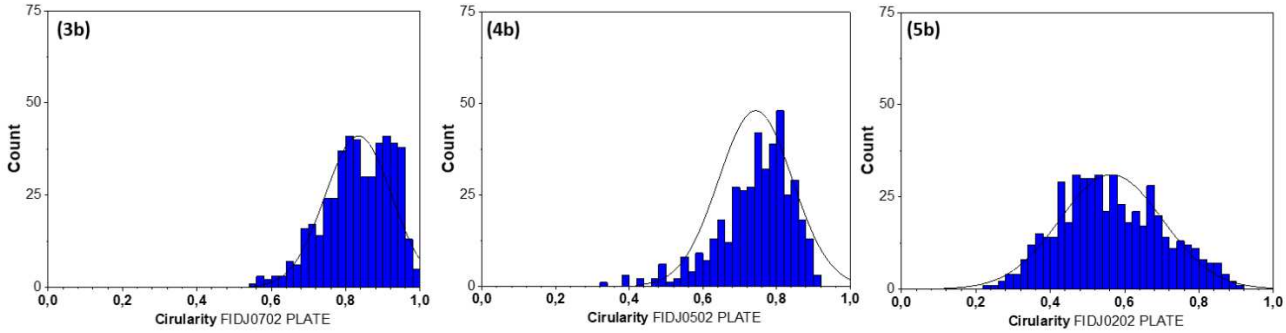

Figure 11: Circularity histograms of plates samples 3b, 4b and 5b.

3.2.3 Coating layer degradation

Figure 10 presents the three different cases of coating degradation corresponding to pullouts from the coating film (chippings), cracks down to the UMo kernel and coating delamination in accordance with observations previously carried out on ZrN coating [18,25,26].

The most frequent degradation mode is film cracking. Radial cracks (Figure 10 for Si-coating and Supplementary Materials for ZrN-coating) nucleate at the surface and propagate from the outside of the film to the substrate as illustrated by the crack growth shape (spike) and by the fact that some cracks do not reach the UMo kernel. The columnar structure of the film, especially for ZrN coating, may promote this mode of crack propagation. Moreover, the curved shape of the substrate and the difference in thermal expansion between coating materials and UMo fuel may boost the bending stress and strain which caused the breaking of the coating. Finally, in some cases, the cracks extend within the UMo substrate by some tens of micrometres (Figure 10 and Supplementary Materials). Longitudinal cracks are visible, they are located at two levels, either in the film itself which gives rise to separation of fragments or they follow the UMo interface giving rise to delamination of the coating from the substrate. The ripping of fragments, which may correspond to an internal delamination, could be raised by the stratified nature of the film in particular for the ZrN coating. The full delamination which can extend over several micrometres, indicates the massive stress induced

by the HR process but also reflects the low adhesion of the film on the substrate. The propagation of a long and wide lateral crack triggered the chippings of the coating large fragments of which are now visible in the Al matrix. As presented in the Supplementary Materials, detailed EDS analyses of delaminated zone show that the film remains mainly attached to the Al matrix and not to the UMo substrate. In this regard, the more fractured surface observed for the annealed UMo kernels (5b) compared to the as-cast UMo ones (3b and 4b), may enhance film degradation.

4 Discussion

Through the use of image analysis techniques and elemental analysis at different scales and energies, a careful examination at successive manufacturing steps of the UMo fuel-plate selected for the international neutron irradiation experiment SEMPER FDELIS, was carried out. The study successively examined the morphology and microstructure of UMo powders coated with ZrN, Mo or Si, through the evaluation of the particle size and shape distributions, as well as a series of metallographic analyses. The results concern the powder atomisation method, *i.e.* by rotating electrode or disk centrifugation, the effect of an additional heat-treatment, the nature of the coating (Si or ZrN) and the effect of hot-rolling process applied for the manufacturing of fuel plates.

The main visible effect of the UMo powder elaboration process concerns their shape. Atomisation using disc centrifugation produces spherical or near-spherical particles, whereas the rotating electrode method yields a significant proportion of elongated particles in addition to near-spherical particles.

The heat treatment has a beneficial effect on the microstructure of the atomised UMo kernels. It is reflected in both the grain structure which is mostly composed of large equiaxed grains,

with a fine and sharp separation at the grain boundaries and in the Mo distribution in the alloy which is found to be uniform. Nevertheless, the heat treatment has an effect on the agglomeration of the particles through the formation of sintering necks which increases particle clustering. Moreover, the heat treatment generates an interaction layer of a few hundred nanometres on the outer part of the UMo kernels. This interface layer, which was studied by STEM, contains U, Mo, C and O, these last two elements being in almost equal proportion. Our measurements show that this interface layer cannot be regarded as essentially composed of UO_2, but that it is a multiphase zone. In agreement with recent analyses [16,34] and examinations by X-ray powder diffraction, the other phases could be uranium carbo-nitrides with possible contamination by oxygen. It should be underlined that the speciation of Mo still remains unknown. This interface layer also has a major influence on the adhesion of the coated layer applied onto the surface of the UMo particles. It is more precisely visible when examining the fuel plate samples. This interface layer seems to be brittle (or at least more brittle that the UMo alloy itself) and its presence deepens the coating degradation during hot-rolling. Through the analysis of the circularity shape factor, our study shows that the contour of the particles is more strongly fragmented for the annealed batch than for the two other non-annealed batches. The fragmentation of the outer zone of the particles leads to more consequent chippings in the Al-matrix, but which may have a limited impact on the irradiation behaviour of the fuel-plates [13].

The coating barriers were examined for different PVD deposited films, Si and ZrN along with some morphological observations on Mo with particular attention paid to their thickness and structure. The thickness was estimated from automated SEM image processing. The radial thickness which typically fall in the range 0.3 and 0.8 µm, increases with the diameter of the UMo kernels. High magnification SEM and TEM images (HAADF images) were used to describe the structure of the deposited films. The Si coating exhibits a heterogeneous structure

comprising a dense columnar layer on the surface of the substrate covered by submicrometric spherules. These spherules that are loosely bonded, define a low compact arrangement with large porosities. This Si film slitting is not considered as harmful for the irradiation performance because silicon easily diffuses through the Al matrix to fill the UMo coating breaches [13,16]. The ZrN film has a typical columnar structure with a growing direction normal to the UMo surface. Nano radial and lateral cracks as well as dimples can be observed. The density of defaults such as cracks, oxygen content, delimitates two sublayers, one denser with less porosities close to the UMo surface and one more porous and with a higher oxygen content close to the Al-matrix. For both deposited films, their cohesion on the substrate is continuous and apparently has a common origin.

The effect of rolling was evaluated for two parameters, the deformation of the UMo kernels and the degradation of the coated film. The evolution of the particle shape assessed using image processing shows a clear evolution of the UMo kernels which mostly lose their spherical shape for faceted and elongated shapes. The deformation rate reaches a value of about 50 to 60%. Another element related to the deformation of the UMo kernels concerns the periphery of the particles which appears strongly fractured, especially for the annealed powder. This surface deformation has a strong impact on the degradation of the deposited film.

Three types of film degradations are visible, cracks, chippings and delamination. The initial structure of the film, particularly the presence of cracks and cavities, appears to act as a nucleation centre for the break of the coating. Both films, ZrN and Si appear with similar degradation rates.

The reasons for the lack of adhesion of the coating to the UMo kernels under the action of massive stresses associated with the HR process were not investigated in the present study, but it could be speculated that both the distinct nature and dissimilar mechanical properties of

the materials involved, as well as the existence of the interface layer on the surface of the substrate alloy, could play a key role in explaining such a behaviour.

5. Conclusion

The present study examined five powders and three fuel-plates selected for the SEMPER FIDELIS experiments at fresh state *i.e.* prior to the neutron irradiation. It focuses on the particles shape, UMo kernel microstructure and coating film features, mainly. As an example, the grain structure of Mo coating was observed for the first time, revealing fibrous columnar structure of the film. Our investigation allows to reveal main features, on the particles morphology depending on the atomisation process, disc centrifugation or rotating electrode, microstructure depending on the metallurgical state of the UMo kernel for as-solidified or annealed powders. The heat-treatment, performed before the coating deposition, promotes the formation of a thin layer at the periphery of the particles comprising U, Mo, C, O and maybe N. This interface layer between the UMo kernel and coated film has strong consequences on the film adhesion especially during the hot-rolling process.

The hot-rolling process has heavy concerns on the deformation of the UMo kernels and the degradation of the coated film. The majority (above 50 %) of UMo kernels lose their spherical shape for faceted and elongated shapes. At this stage, no relationship between the shape distortion rate and the metallurgical state of the UMo kernels *i.e*. as-solidified or annealed has been demonstrated. Homogenization annealing clearly demonstrates its efficiency for the uniform distribution of the Mo within the particles, but the resulting grain structure shows large equiaxed grains with some grain subdivisions (subgrains) which is known to soften metallic materials favouring easy deformation under constrain. Film degradation is classified into three effects; cracks, chippings and delamination. Origin of the film deterioration by HR process was not investigated in the present study, but characterisation of UMo kernel

mechanical properties, including strain analysis and texture evolution, are currently under investigation.

Acknowledgement

The authors would like to thank KAERI (Korean Atomic Energy Research Institute) for producing and supplying the U-Mo powders produced by centrifugal atomisation. This project has received funding from the EURATOM research and training program 2014-2018 under grant agreement no.661935.

Chevreul Institute (FR 2638), Ministère de l'Enseignement Supérieur, de la Recherche et de l'Innovation, Hauts-de-France Region and FEDER are acknowledged for supporting and partial funding of this work. E. Callarec and A. Rolland are warmly thanked for their careful preparation of the samples as well as their strong involvement in the SEM images collection. The authors are grateful to D. Troadec (IEMN lab) for the preparation of the fibbed lamella.

Credit Author Statement

Mira Khair: Investigation, Formal Analysis, Writing. François Housaer: Methodology, Investigation, Formal Analysis. Nicolas Hibert : Investigation, Review and Editing. Jérôme Allenou: Conceptualisation, Methodology, Review and Editing. Ahmed Addad: Investigation, Analysis, Review and Editing. Franck Beclin: Conceptualisation, Methodology, Investigation, Analysis, Review and Editing. Matthieu. Touzin: Conceptualisation, Methodology, Investigation, Analysis, Review and Editing. Ann Leenaers: Conceptualisation, Investigation, Review and Editing, Supervision. Hervé Palancher: Conceptualisation, Review and Editing. Bertrand Stepnik: Conceptualisation, Methodology, Review and Editing, Supervision. Olivier

Tougait: Methodology, Investigation, Formal Analysis, Writing – Original Draft, Review and Editing, Supervision.

Declaration of interests

The authors declare that they have no known competing financial interests or personal relationships that could have appeared to influence the work reported in this paper.

6. References

[1] J.L. Snelgrove, G.L. Hofman, M.K. Meyer, C.L. Trybus, T.C. Wiencek, Development of very-high-density low-enriched-uranium fuels, Nucl. Eng. Des. 178 (1997) 119–126. https://doi.org/10.1016/S0029-5493(97)00217-3.

[2] S. Van den Berghe, P. Lemoine, Review of 15 years of high-density lowenriched UMo dispersion fuel development for research reactors in Europe, Nucl. Eng. Technol. 46 (2014) 125–146. https://doi.org/10.5516/NET.07.2014.703.

[3] M.K. Meyer, G.L. Hofman, S.L. Hayes, C.R. Clark, T.C. Wiencek, J.L. Snelgrove, R. V. Strain, K.H. Kim, Low-temperature irradiation behavior of uranium-molybdenum alloy dispersion fuel, J. Nucl. Mater. 304 (2002) 221–236. https://doi.org/10.1016/S0022-3115(02)00850-4.

[4] F. Huet, V. Marelle, J. Noirot, P. Sacristan, P. Lemoine, Full-Sized Plates Irradiation With High UMo Fuel Loading - Final Results Of IRIS 1 Experiment, Int. Meet. Reduc. Enrich. Res. Test React. (2003) 1–10. https://inis.iaea.org/collection/NCLCollectionStore/_Public/35/066/35066241.pdf.

[5] S. Van den Berghe, W. Van Renterghem, A. Leenaers, Transmission electron microscopy investigation of irradiated U-7 wt%Mo dispersion fuel, J. Nucl. Mater. 375 (2008) 340–346. https://doi.org/10.1016/j.jnucmat.2007.12.006.

[6] S. Van den Berghe, Y. Parthoens, F. Charollais, Y.S. Kim, A. Leenaers, E. Koonen, V. Kuzminov, P. Lemoine, C. Jarousse, H. Guyon, D. Wachs, D. Keiser, A. Robinson, J. Stevens, G. Hofman, Swelling of U(Mo)-Al(Si) dispersion fuel under irradiation-Non-destructive analyses of the LEONIDAS E-FUTURE plates, J. Nucl. Mater. 430 (2012) 246–258. https://doi.org/10.1016/j.jnucmat.2012.06.045.

[7] H.J. Ryu, J.S. Park, J.M. Park, C.K. Kim, The effect of Si-rich layer coating on U-Mo vs. Al interdiffusion, Nucl. Eng. Technol. 43 (2011) 159–166. https://doi.org/10.5516/NET.2011.43.2.159.

[8] A. Leenaers, S. Van den Berghe, E. Koonen, V. Kuzminov, C. Detavernier, Fuel swelling and interaction layer formation in the SELENIUM Si and ZrN coated U(Mo) dispersion fuel plates irradiated at high power in BR2, J. Nucl. Mater. 458 (2015) 380–393. https://doi.org/10.1016/j.jnucmat.2014.12.073.

[9] H.-Y. Chiang, T. Wiss, S.-H. Park, O. Dieste-Blanco, W. Petry, TEM analysis of irradiation-induced interaction layers in coated UMo/X/Al trilayer systems (X= Ti, Nb, Zr, and Mo), J. Nucl. Mater. 499 (2018) 558–566. https://doi.org/10.1016/j.jnucmat.2017.12.015.

[10] S. Kim, Y.S. Kim, Y.J. Jeong, K. Mo, Y. Miao, B. Ye, A. Oaks, S. Bhattacharya, K.H. Lee, K.N. Kim, J.M. Park, A.M. Yacout, Effectiveness of the metal coating on U–7Mo dispersion fuel in Al during irradiation, J. Nucl. Mater. 529 (2020). https://doi.org/10.1016/j.jnucmat.2019.151945.

[11] A. Leenaers, W. Van Renterghem, S. Van den Berghe, High burn-up structure of U(Mo) dispersion fuel, J. Nucl. Mater. 476 (2016) 218–230. https://doi.org/10.1016/j.jnucmat.2016.04.035.

[12] B.D. Miller, D.D. Keiser, M. Abir, A. Aitkaliyeva, A. Leenaers, B.J. Hernandez, W. Van Renterghem, A. Winston, 3D reconstructions of irradiated U–Mo fuel to understand breaching effects in ZrN diffusion barriers, J. Nucl. Mater. 510 (2018) 431–

436. https://doi.org/10.1016/j.jnucmat.2018.08.016.

[13] W. Van Renterghem, B.D. Miller, A. Leenaers, S. Van den Berghe, J. Gan, J.W. Madden, D.D. Keiser, Transmission electron microscopy investigation of neutron irradiated Si and ZrN coated UMo particles prepared using FIB, J. Nucl. Mater. 498 (2018) 60–70. https://doi.org/10.1016/j.jnucmat.2017.10.016.

[14] D. Jadernas, J. Gan, D. Keiser, J. Madden, M. Bachhav, J.-F. Jue, A. Robinson, Microstructural characterization of as-fabricated and irradiated U-Mo fuel using SEM/EBSD, J. Nucl. Mater. 509 (2018) 1–8. https://doi.org/10.1016/j.jnucmat.2018.06.007.

[15] B. Stepnik, M. Grasse, C. Rontar, D. Geslin, Y. Guinard, S. Van den Berghe, A. Leenaers, H. Breitkreutz, W. Petry, H. Palancher, E. Hervieu, Y. Calzavara, H. Guyon, Manufacturing of the SEMPER FIDELIS UMo irradiation experiment (RRFM Conference) Proceedings of the 22sd International Meeting on Research Reactor Fuel Management, Munich, Germany, (2018).

[16] A. Leenaers, B. Ye, J. Van Eyken, S. Van den Berghe, ZrN coating as diffusion barrier in U(Mo) dispersion fuel systems, J. Nucl. Mater. 552 (2021) 153000. https://doi.org/10.1016/j.jnucmat.2021.153000.

[17] F. Housaer, F. Vanni, M. Touzin, F. Béclin, J. Allenou, A. Leenaers, A.M. Yacout, H. Palancher, B. Stepnik, O. Tougait, Morphological characterization of the fresh ZrN coated UMo powders used in EMPIrE irradiation experiment: A practical approach, J. Nucl. Mater. 533 (2020). https://doi.org/10.1016/j.jnucmat.2020.152087.

[18] X. Iltis, H. Palancher, J. Allenou, F. Vanni, B. Stepnik, A. Leenaers, S. Van Den Berghe, D.D. Keiser, I. Glagolenko, Characterization of fresh EMPIrE and SEMPER FIDELIS U(Mo)/Al fuel plates made with PVD-coated U(Mo) particles, EPJ Nucl. Sci. Technol. 4 (2018) 49. https://doi.org/10.1051/epjn/2018048.

[19] K.H. Kim, D.B. Lee, C.K. Kim, G.E. Hofman, K.W. Paik, Characterization of U-2 wt% Mo and U-10 wt% Mo alloy powders prepared by centrifugal atomization, J. Nucl. Mater. 245 (1997) 179–184. https://doi.org/10.1016/S0022-3115(97)00011-1.

[20] R. Schenk, W. Petry, B. Stepnik, C. Jarousse, G. Bourdat, C. Moyoud, M. Grasse, RRFM Conference _ Proceedings of the 17th International Meeting on Research Reactor Fuel Management, Saint-Petersbourg, Russia, (2013).

[21] A. Leenaers, S. Van den Berghe, C. Detavernier, Surface engineering of low enriched uranium-molybdenum, J. Nucl. Mater. 440 (2013) 220–228. https://doi.org/10.1016/j.jnucmat.2013.04.068.

[22] C.A. Schneider, W.S. Rasband, K.W. Eliceiri, NIH Image to ImageJ : 25 years of image analysis, Nat. Methods. 9 (2012) 671–676. https://doi.org/10.1038/nmeth.2089.

[23] J. Rodriguez-Carvajal, Recent Developments of the Program FULLPROF, in Newsletter of the Commission on Powder Diffraction (IUCr), 26 (2001) 12–19. http://journals.iucr.org/iucr-top/comm/cpd/Newsletters/.

[24] F. Sondej, A. Bück, E. Tsotsas, Comparative analysis of the coating thickness on single particles using X-ray micro-computed tomography and confocal laser-scanning microscopy, Powder Technol. 287 (2016) 330–340. https://doi.org/10.1016/j.powtec.2015.09.039.

[25] J.-H. Kim, G.Y. Jeong, S. Kim, Y.J. Jeong, J.M. Park, D.-S. Sohn, Dependence of thickness, morphology, and crystallographic properties of Mo and ZrN coatings on U-

Mo substrate size, J. Nucl. Mater. 512 (2018) 156–168. https://doi.org/10.1016/j.jnucmat.2018.10.012.

[26] D.D. Keiser Jr., E. Perez, T. Wiencek, A. Leenaers, S. Van den Berghe, Microstructural characterization of a thin film ZrN diffusion barrier in an As-fabricated U-7Mo/Al matrix dispersion fuel plate, J. Nucl. Mater. 458 (2015) 406–418. https://doi.org/10.1016/j.jnucmat.2014.12.036.

[27] J.-H. Kim, G.Y. Jeong, S. Kim, Y.J. Jeong, D.-S. Sohn, Effect of coating thickness and annealing temperature on ZrN coating failure of U-Mo particles under heat treatment, J. Nucl. Mater. 507 (2018) 347–359. https://doi.org/10.1016/j.jnucmat.2018.05.019.

[28] L. He, M. Bachhav, D.D. Keiser, J.W. Madden, E. Perez, B.D. Miller, J. Gan, W. Van Renterghem, A. Leenaers, S. Van den Berghe, STEM-EDS/EELS and APT characterization of ZrN coatings on UMo fuel kernels, J. Nucl. Mater. 511 (2018) 174–182. https://doi.org/10.1016/j.jnucmat.2018.09.004.

[29] J.M. Park, H.J. Ryu, K.H. Kim, D.B. Lee, Y.S. Lee, J.S. Lee, B.S. Seong, C.K. Kim, M. Cornen, Neutron diffraction analyses of U-(6-10 wt.%)Mo alloy powders fabricated by centrifugal atomization, J. Nucl. Mater. 397 (2010) 27–30. https://doi.org/10.1016/j.jnucmat.2009.11.026.

[30] X. Iltis, I. Zacharie-Aubrun, H.J. Ryu, J.M. Park, A. Leenaers, A.M. Yacout, D.D. Keiser, F. Vanni, B. Stepnik, T. Blay, N. Tarisien, C. Tanguy, H. Palancher, Microstructure of as atomized and annealed U-Mo7 particles: A SEM/EBSD study of grain growth, J. Nucl. Mater. 495 (2017) 249–266. https://doi.org/10.1016/j.jnucmat.2017.07.056.

[31] R. Jungwirth, H. Palancher, A. Bonnin, C. Bertrand-Drira, C. Borca, V. Honkimäki, C. Jarousse, B. Stepnik, S.H. Park, X. Iltis, W.W. Schmahl, W. Petry, Microstructure of as-fabricated UMo/Al(Si) plates prepared with ground and atomized powder, J. Nucl. Mater. 438 (2013) 246–260. https://doi.org/10.1016/j.jnucmat.2013.03.021.

[32] T. Zweifel, H. Palancher, A. Leenaers, A. Bonnin, V. Honkimaki, R. Tucoulou, S. Van Den Berghe, R. Jungwirth, F. Charollais, W. Petry, Crystallographic study of Si and ZrN coated U-Mo atomised particles and of their interaction with Al under thermal annealing, J. Nucl. Mater. 442 (2013) 124–132. https://doi.org/10.1016/j.jnucmat.2013.08.050.

[33] S. Bhattacharya, L. Jamison, D.N. Seidman, W. Mohamed, Y. Bei, M.J. Pellin, A.M. Yacout, Nanocrystalline ZrN thin film development via atomic layer deposition for U-Mo powder, J. Nucl. Mater. 526 (2019) 151770. https://doi.org/10.1016/j.jnucmat.2019.151770.

[34] T. Ajantiwalay, C. Smith, D.D. Keiser, A. Aitkaliyeva, A critical review of the microstructure of U–Mo fuels, J. Nucl. Mater. 540 (2020) 152386. https://doi.org/10.1016/j.jnucmat.2020.152386.

[35] W.J. Siekhaus, P.K. Weber, I.D. Hutcheon, J.E.P. Matzel, W. McLean, Hydrogen accumulation in and at the perimeter of U-C-N-O inclusions in uranium - A SIMS analysis, J. Alloys Compd. 645 (2015) S225–S229. https://doi.org/10.1016/j.jallcom.2015.01.050.

[36] M. Guthrie, C.J. Benmore, L.B. Skinner, O.L.G. Alderman, J.K.R. Weber, J.B. Parise, M. Williamson, Thermal expansion in UO2 determined by high-energy X-ray diffraction, J. Nucl. Mater. 479 (2016) 19–22.

https://doi.org/10.1016/j.jnucmat.2016.06.042.

[37] I. Seiichi, S. Motokazu, A. Yumi, High-temperature thermal lattice expansion of mixed carbo-nitride and uranium carbo-nitride, J. Nucl. Mater. 39 (1971) 311–314. https://doi.org/10.1016/0022-3115(71)90150-4.

[38] A.E. Austin, A.F. Gerds, The Uranium-Nitrogen-Carbon System (Report No. BMI-1272 _ UC-25 Metallurgy and Ceramics _ TID-4500, 13th Ed., Rev.), Battelle Meml. Inst. (1958). https://www.osti.gov/servlets/purl/4300790.

Graphical Abstract

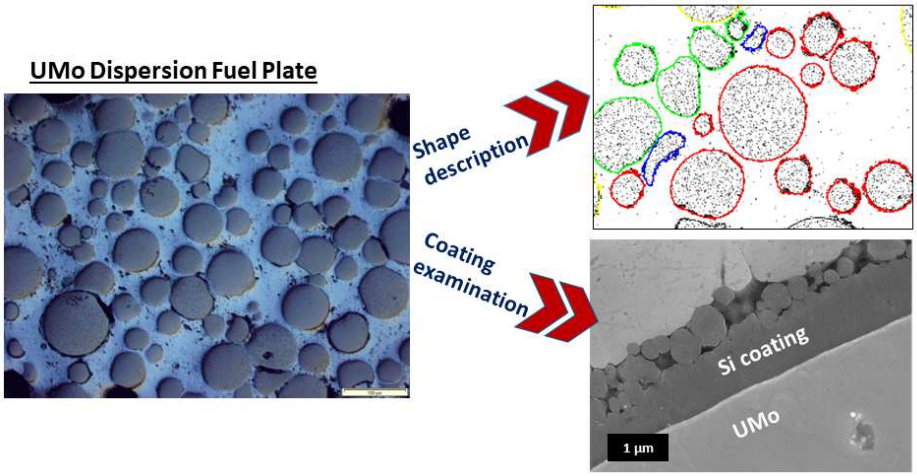

Highlights

- Fuel-plates of the SEMPER FIDELIS irradiation test were characterized.
- Influence of successive manufacturing steps was examined
- Chemical composition at UMo-ZrN interface was carried out.
- Coating and UMo kernel microstructures were investigated.
- Grain-structure of Mo coating is presented for the first time.